Quantification of Electroporative Uptake Kinetics and Electric Field Heterogeneity Effects in Cells

S. M. Kennedy, Z. Ji, J. C. Hedstrom, J. H. Booske, and S. C. Hagness
Department of Electrical and Computer Engineering, University of Wisconsin, Madison, Wisconsin 53706

ABSTRACT We have conducted experiments quantitatively investigating electroporative uptake kinetics of a fluorescent plasma membrane integrity indicator, propidium iodide (PI), in HL60 human leukemia cells resulting from exposure to 40 μs pulsed electric fields (PEFs). These experiments were possible through the use of calibrated, real-time fluorescence microscopy and the development of a microcuvette: a specialized device designed for exposing cell cultures to intense PEFs while carrying out real-time microscopy. A finite-element electrostatic simulation was carried out to assess the degree of electric field heterogeneity between the microcuvette's electrodes allowing us to correlate trends in electroporative response to electric field distribution. Analysis of experimental data identified two distinctive electroporative uptake signatures: one characterized by low-level, decelerating uptake beginning immediately after PEF exposure and the other by high-level, accelerating fluorescence that is manifested sometimes hundreds of seconds after PEF exposure. The qualitative nature of these fluorescence signatures was used to isolate the conditions required to induce exclusively transient electroporation and to discuss electropore stability and persistence. A range of electric field strengths resulting in transient electroporation was identified for HL60s under our experimental conditions existing between 1.6 and 2 kV/cm. Quantitative analysis was used to determine that HL60s experiencing transient electroporation internalized between 50 and 125 million nucleic acid-bound PI molecules per cell. Finally, we show that electric field heterogeneity may be used to elicit asymmetric electroporative PI uptake within cell cultures and within individual cells.

INTRODUCTION

A cell membrane may become permeable to a variety of normally membrane-impermeable molecules in the presence of an externally applied pulsed electric field (PEF). This permeability is attributed commonly to the development of electrically-induced membrane pores, or electropores (1–4). Electroporation may be used to damage or destroy unwanted cells, for instance, through the induction of necrotic (5–7) and apoptotic (8–11) death. Electroporation may also be used to deliver a number of important, biologically-active molecules to cells such as peptides, full-length proteins, siRNA, mRNA, and DNA (4,12,13) providing great flexibility in modifying cell behaviors. However, for these molecules to maintain their biological and therapeutic potentials, the cell must remain viable after exposure to a potentially traumatic PEF. This, in turn, requires that induced electropores exist only temporarily (i.e., induction of transient electroporation). Electroporation has been applied successfully for decades as a gene and drug delivery technique (14–17). However, despite its ubiquitous use, much remains unknown regarding the underlying mechanisms of electroporation and the ensuing molecular transport across the plasma membrane. Specifically, the rate, duration, and total amount of uptake (i.e., the uptake kinetics) need to be well characterized.

There have been a number of numerical investigations focusing on the dynamics and mechanisms behind electroporation and the ensuing uptake of exogenous molecules (18–23). However, there are a limited number of experimental investigations attempting to characterize electroporative uptake kinetics, particularly in a quantitative manner. Such experimental studies remain a high priority in electroporation research (18). Experimental investigations examining electroporative uptake kinetics require real-time observation of cells during and after electric field exposure and use of quantitatively calibrated microscopy. We carried out real-time, quantitative experiments characterizing electroporatively induced propidium iodide (PI) uptake in HL60 human leukemia cells when exposed to 40 μs PEFs. The experimental data obtained here are used to address a number of important issues regarding the dynamics of electroporatively-induced molecular uptake. Specifically, these data are used to show the effects of electric field heterogeneity within a suspended cell culture and in individual cells, characterize the nature of molecular uptake during transient and irreversible electroporation, identify a range of field strengths resulting in exclusively transient electroporation (i.e., a transient electroporation window), and estimate the number of molecules internalized during transient electroporation. We also show the exploitation of field heterogeneity to spatially regulate electroporative uptake that may be useful in a number of biomedical applications.

The experiments presented here provide data required to validate and improve existing numerical simulation models designed to describe electroporation and electroporative uptake. This study also underscores the need for future experimental studies designed to determine the influence of PEF duration, PEF intensity, PEF shape (waveform characteris-

Submitted December 15, 2006, and accepted for publication February 20, 2008.

Address reprint requests to S. M. Kennedy, E-mail: smkennedy@wisc.edu.

Editor: Eduardo Perozo.

0006-3495/08/06/5018/10 $2.00

doi: 10.1529/biophysj.106.103218

tics), PEF number and separation time, molecular size, molecular structure, and environmental conditions on electroporative uptake kinetics, which are critical steps in optimizing the efficacy of electroporation technology in biological research and medicine.

MATERIALS AND METHODS

Microcuvette

A description of the microcuvette's fabrication is provided in the Appendix. An en face view of a completed microcuvette is provided in Fig. 1 *a*. The edges of the electrodes are slightly rounded at each end of the electrode gap to prevent electrical arcing when intense voltages are applied (Fig. 1 *b*). An electrode spacing of 80 μm was achieved (Fig. 1 *c*) with 24 subsequent reproductions yielding electrode separations of 80 ± 4 μm. Electrode heights were 19 ± 5 μm. These microcuvettes have proven to be quite robust. A single microcuvette with an 80-μm electrode gap and an electrode height of 19 μm was used in (23) and in this current investigation. The same microcuvette has remained completely viable after hundreds of experimental trials.

As described in the Appendix, nickel electrodes are used in the microcuvette due to convenience in fabrication. The potential cytotoxic effect of nickel molecules liberated from the electrodes during PEF exposure is not addressed here. The focus of this work is to quantitatively characterize PEF-induced molecular uptake of a membrane integrity indicator over a relatively short period of time (hundreds of seconds). The time frame associated with the toxicity of internalized nickel molecules having an effect on plasma membrane integrity is likely longer than the hundreds of seconds post-electroporation examined here. However, because it has been shown that i), free nickel molecules have a cytotoxic effect on cells when internalized endocytically (24); and ii), the cytotoxic effect of molecules normally internalized endocytically is amplified in electroporated cells (25), nickel toxicity will be a concern moving forward when examining long-term electroporative effects in cells. It should be noted that any metal capable of electroplating may be used to construct the microcuvette's electrodes. In future studies, the microcuvette's electrodes will be constructed using a biologically inert metal such as gold.

Finite-element electrostatics simulation

We analyzed the electrical field distribution in the microcuvette's electrode gap using FEMLAB (COMSOL, Burlington, MA), a finite-element model (FEM) software package, for the case of 1 V excitation across the electrodes. This was done to assess the degree of electric field heterogeneity between the microcuvette's electrodes. The cell buffer was modeled using a dielectric constant of 78, which may vary depending on the buffer's ionic concentration, and the glass microscope slide was modeled using a dielectric constant of 4.6. The total simulation area was set large enough compared to the electrode gap area to obtain accurate electric field data in the microcuvette's electrode gap. The data obtained from this FEM simulation do not consider the overvoltages at the metal-electrolyte interface and therefore may be overestimates of the actual electrolytic electric field intensities that would be produced in the microcuvette's electrode gap upon voltage excitation. Nevertheless, the electric field patterns obtained from this simulation do adequately characterize the electric field heterogeneity in the microcuvette's electrode gap and will be used to describe the distribution in cellular response during PEF exposure experiments based on the location of cells within the electrode gap. Future studies will either quantify the Ni-electrolyte overvoltage to determine actual electrolytic electric fields or use electrode materials where overvoltage is known to be less of an issue (e.g., silver–silver chloride).

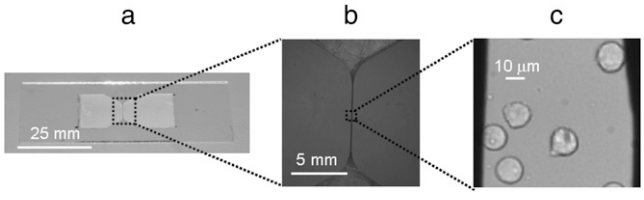

FIGURE 1 (*a*) Image of completed microcuvette. (*b*) Image under low magnification detailing arc-preventing electrode curvature. (*c*) Image under 40× magnification detailing HL60s resting between the microcuvettes.

PEF electronics and microscopy setup

PEFs were applied to the cells by applying voltage pulses across the microcuvette's electrodes using a gated high-voltage system. The applied voltage was set and supplied from a Glassman ER series 3200 W regulated high-voltage DC power supply (Glassman High Voltage, High Bridge, NJ). This DC voltage was gated using a DEI Model PVX-4150 high-speed switch (Directed Energy, Fort Collins, CO) triggered by a Model 555 two-channel pulse/delay generator (Berkeley Nucleonics, San Rafael, CA). This electrical system was capable of creating square voltage pulses up to 1.5 kV with pulse widths as short as 60 ns. Using a microcuvette loaded with cells suspended in Hanks' balanced salt solution (HBSS), the maximum nominal electric fields within the 80-μm electrode gap were on the order of 90 kV/cm. The pulse rise and fall times (to reach 90% of final value) were $\tau_r = 64$ ns and $\tau_f = 70$ ns, respectively (see Fig. 2 for a representative waveform used in these studies). The voltage applied across the electrodes was monitored using a Tektronix 2221A digital storage oscilloscope (Tektronix, Richardson, TX)

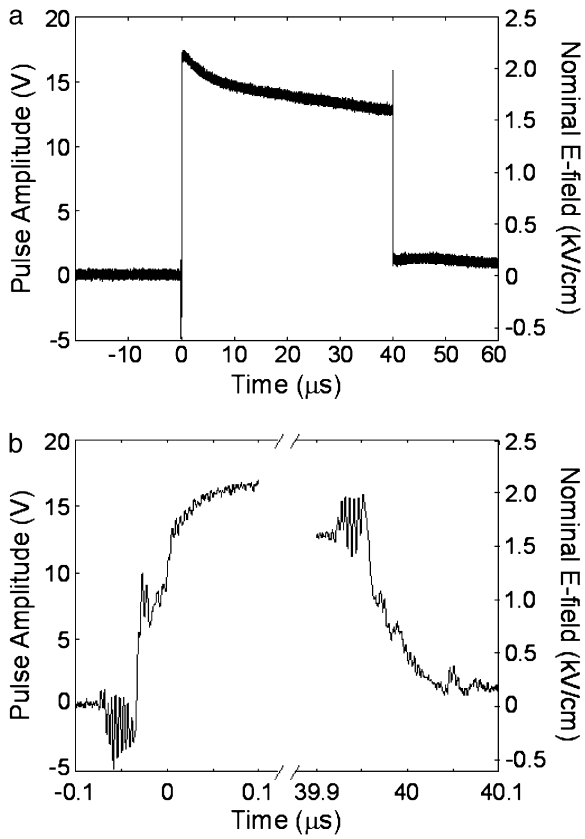

FIGURE 2 (*a*) PEF waveform (40 μs) taken from digital oscilloscope. (*b*) A zoomed-in plot detailing PEF rise and fall times.

and was used to determine the nominal electric field value between the microcuvette's electrodes.

Real-time image acquisition during experimentation was achieved using a Nikon Eclipse TE200 inverted microscope (Nikon USA, Melville, NY) equipped with a Hamamatsu C4742-95 Digital charge-coupled device (CCD) camera (Hamamatsu Photonics, Bridgewater, NJ). A schematic of the electrical delivery and microscopy setup can be seen in Fig. 3. Fluorescence microscopy was used to monitor the fluorescence of internalized, nucleic acid-bound propidium iodide (PI). Filters were selected to excite nucleic acid-bound PI at 535 nm using a Lambda DG-4 excitation lamp/high speed wavelength switcher (Sutter Instrument, Novato, CA) and monitor its fluorescence at 617 nm. Control and timing of the excitation lamp and CCD camera were provided by PC software (Prairie Technologies, Madison, WI). Data extraction from acquired images was carried out in MATLAB (The MathWorks, Natick, MA). CCD camera exposure time and gain settings were optimally set, establishing sensitivities appropriate for investigating different levels of molecular uptake.

Cell maintenance, preparation, and experimental protocol

All PEF exposure experiments examined the response of HL60 human promyelocytic leukemia cells (American Type Culture Collection, Manassas, VA). HL60s were cultured in RPMI-1640 containing 2% glutamine supplemented with 10% fetal bovine serum and 2% penicillin and streptomycin at 37°C and 5% CO_2. Before experimentation, cells were resuspended in HBSS without Phenol Red, Ca^{2+} and Mg^{2+} via centrifugal washing (1000 rpm for 5 min at 27°C). Cell concentration was set between 1 million and 2 million cells/ml. The HBSS conductivity was measured as 1.424 S/m using an Orion model 160 conductivity meter (Orion Research, Beverly, MA). PI (Fisher Scientific International, Pittsburgh, PA), a fluorescent plasma membrane integrity indicator, was added to the cell-HBSS mixture to form a PI concentration of 30 μM in the experimental medium. PI is normally membrane impermeable and will traverse cellular membranes only when membrane integrity has been compromised. Once PI molecules have penetrated the plasma membrane they will bind to available intracellular nucleic acids, dramatically increasing their fluorescence capacity.

A microcuvette was prepared for experiments by placing a nylon washer over the electrode gap to provide a well for the HBSS/cell/PI experimental medium; 12 μL of medium was then placed in the well and a microscope coverslip was placed on top to limit evaporation during experimentation. The two electrodes of the microcuvette were electrically connected to the gated PEF electronics and an oscilloscope probe was connected across the two connections. The cells were allowed to settle between the microcuvette's electrodes for 10 min. Fluorescence microscopy data acquisition was initialized 1 min before PEF application. One fluorescent image was acquired every 5 s for 10 min.

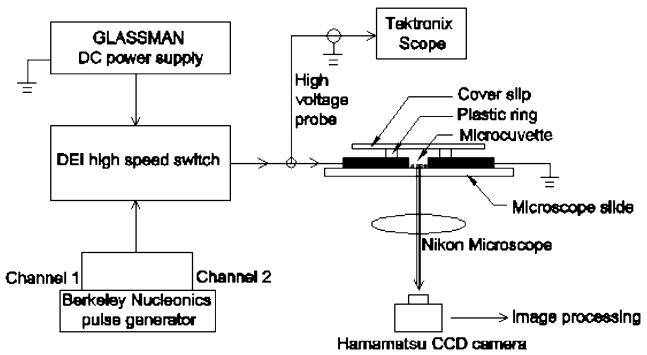

FIGURE 3 Schematic of gated high-voltage PEF delivery system, cell exposure microcuvette, microscopy setup, and microscope image acquisition system.

To obtain cellular PI fluorescence intensities associated with permanent membrane permeability, cells were chemically lysed using saponin (Alfa Aesar, Ward Hill, MA) at 0.2% with 30 μM of extracellular PI. These fluorescence intensities were used in analyzing electropore persistence in a similar manner to (26).

Fluorescence microscopy calibration

A calibration of the fluorescence microscopy system was carried out to correlate an individual cell's fluorescence intensity to an estimated number of internalized, nucleic acid-bound PI molecules. A known quantity of cells were chemically lysed in 0.2% saponin with known quantities of available PI and examined under fluorescence microscopy. In individual experiments with different known quantities of available PI, the mean arbitrary fluorescence intensity of ~30 cells was recorded. With the known number of cells, the numbers of intercellular, bound PI molecules per cell were estimated by dividing the number of available PI molecules by the total number of cells. This method provides accurate results as long as the number of available PI molecules is small compared with the number of intracellular PI binding sites.

Using a 300-ms camera exposure time, the mean cellular fluorescence intensity increased linearly as the amount of available PI increased (Fig. 4 *a*, Region I). This is consistent with there being plenty of intracellular PI binding sites. Therefore, the linear region of the calibration curve provides an accurate estimate relating an individual cell's fluorescence intensity to the number of internalized, bound PI molecules. However, as the quantity of

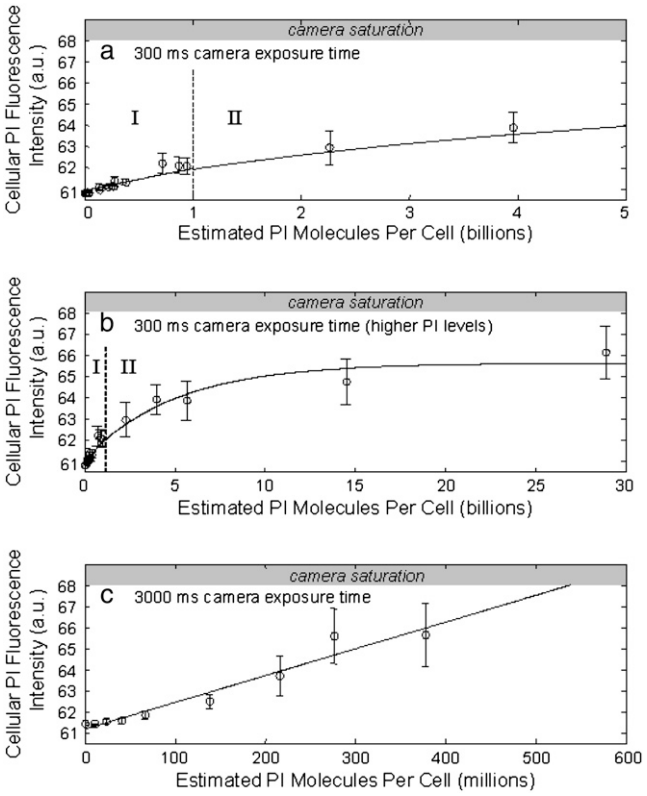

FIGURE 4 Fluorescence microscopy calibration curves. (*a*) The beginning of the calibration curve corresponding to a 300 ms camera exposure time for low values of estimated internalized PI molecules. Regions I and II indicate linear versus exponential curve fitting, respectively. (*b*) The full 300 ms exposure time calibration curve that is mostly nonlinear. (*c*) The calibration curve corresponding to a 3000 ms exposure time for heightened sensitivity.

available PI was increased, mean cellular fluorescence intensity began saturating (Fig. 4 *a*, Region II). This is consistent with a reduction in intracellular PI binding sites due to an abundance of available PI. As these binding sites become increasingly unavailable the calibration curve becomes increasingly inaccurate (i.e., as the calibration curve asymptotes, it becomes less accurate). However, as will be discussed later, the linear region of the calibration curve will be useful in accurately estimating the limited number of internalized PI molecules during transient electroporation. The complete calibration curve for 300 ms camera exposure times is provided in Fig. 4 *b*.

To detect smaller quantities of internalized PI, the microscopy system is also calibrated using a more sensitive setting: a camera exposure time of 3000 ms. Again, the mean cellular fluorescence intensity increased linearly as the amount of available PI increased (Fig. 4 *c*). However, at this increased sensitivity, the camera saturates before the calibration curve develops asymptotic characteristics, providing a sensitive and accurate calibration. The experiments described here will use this calibration curve (Fig. 4 *c*) to correlate cellular fluorescence intensity to a number of internalized, bound PI molecules.

RESULTS

FEM electrostatic simulation results

An FEM simulation was conducted to characterize the electric field heterogeneity within the microcuvette's electrode gap. The microcuvette used in these experiments had an electrode spacing of 80 μm and an electrode height of 19 μm. The result of this simulation is provided in Fig. 5 *a* in the form of a contour plot that shows the electric field distribution between the electrodes of the microcuvette in the case of 1 V electrode excitation. The nominal electric field (E_n) is the electrode voltage divided by the electrode spacing and its contour is plotted in bold. Contours other than E_n are spaced 2000 V/m (0.02 kV/cm) apart.

In Fig. 5 *b*, a cartoon of an HL60 is provided illustrating its approximate size relative to electric field gradients between the microcuvette's electrodes. The E_n contours along with the vertical dimension of an HL60 cell conveniently divides the microcuvette's electrode gap into two regions: Region I in the middle 56% of the electrode gap and Region II in the remaining part of the electrode gap near either electrode. In Region I, the simulated electric field varies between 0.87 E_n and E_n whereas in Region II, the electric field varies between E_n and 1.27 E_n. Although the value of E_n is not necessarily the actual electrolytic electric field, it will nevertheless be useful in characterizing observed HL60 electroporative responses. Specifically, this electrostatic simulation shows that cells lying in Region I will be exposed to field intensities slightly less than the nominal electric field value whereas, cells lying in Region II will be exposed to slightly higher field values.

PI uptake experimental results

PEF-induced PI uptake was monitored in real-time using fluorescence microscopy for HL60s exposed to 40 μs PEFs of varying amplitudes. Results from experiments using nominal PEF intensities (E_n) of 0, 1.60 and 2.05 kV/cm are shown in Fig. 6, *a–c*, respectively. To monitor cellular fluorescence at low levels, the data in Fig. 6 were taken using high camera sensitivity (exposure time = 3000 ms). Increasing camera exposure time further provided no additional insight regarding observation of low-level PI uptake (i.e., no PI uptake was observed at lower PEF intensities). In Fig. 6, *a–c*, individual curves represent PI fluorescence intensity over time for individual cells. This fluorescence intensity is shown in arbitrary units (a.u.) on the left vertical axis. On the right vertical axis, an estimate of the number of internalized PI molecules is provided using the calibration curve shown in Fig. 4 *c*. In the included discussion, we will use these calibrated data under the assumption that they are accurate estimates of the number of internalized, bound PI molecules per cell. Solid lines represent individual cells in the middle 56%

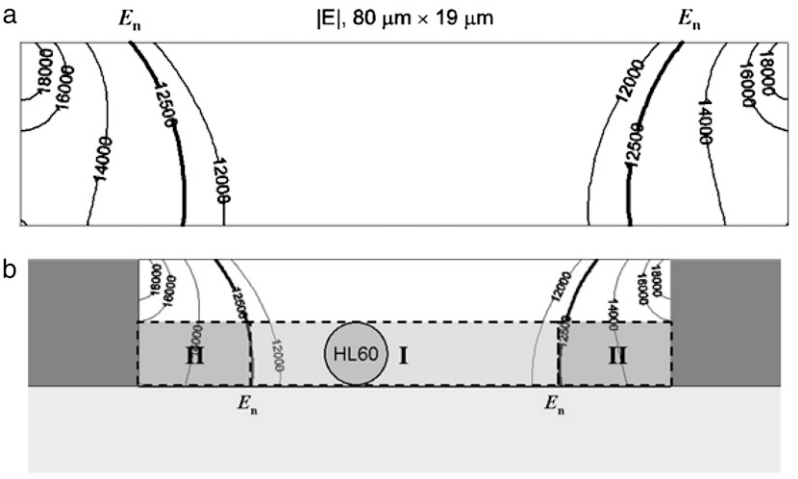

Electrode Gap Dimensions Width x Height (μm)	Electric Field Variation In Middle 56% of Electrode Gap (Region I)	Electric Field Variation Near Electrodes (Region II)
80 x 19	$0.87E_n < \|E\| < E_n$	$E_n < \|E\| < 1.27\ E_n$

FIGURE 5 (*a*) FEM simulation data describing the field nonuniformity between the microcuvette's electrodes. The bold contour indicates the nominal electric field value E_n computed as the applied voltage divided by the electrode separation distance. All other contours are 0.02 kV/cm apart. (*b*) Image detailing how the location of the nominal field contours and the average diameter of an HL60 conveniently divides the area between the electrodes into two regions: Region I where field intensities are $<E_n$ and Region II where intensities are $>E_n$. (*Table*) Summary of the (nonelectrolytic) field intensities expected in the microcuvette used in these electroporation experiments.

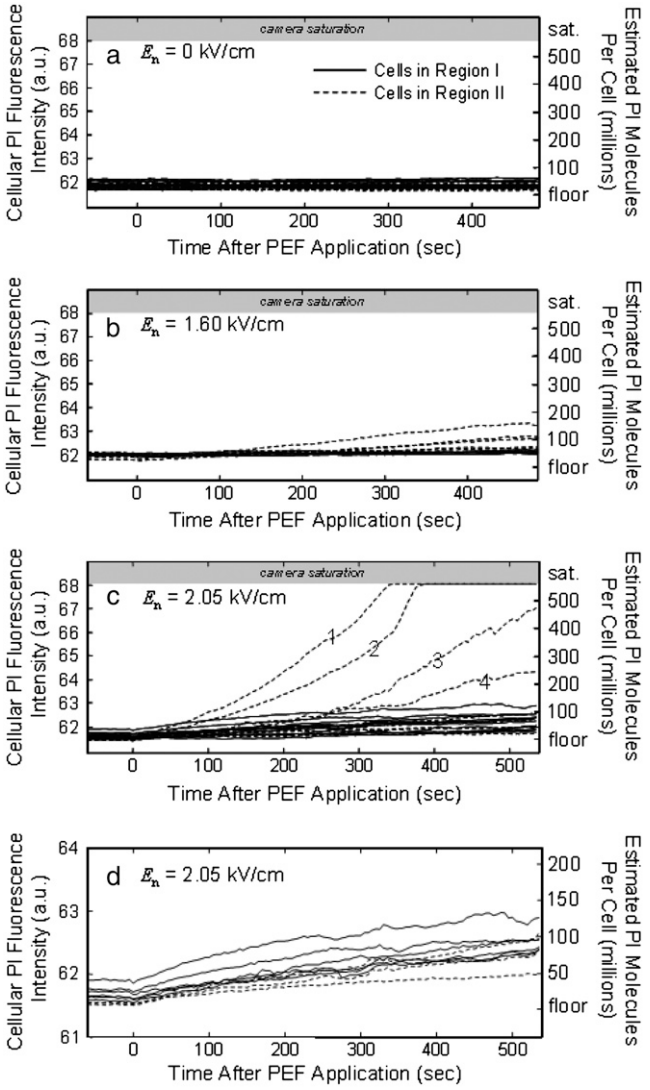

FIGURE 6 PI fluorescence versus time for individual HL60s when exposed to 40 μs PEFs with nominal intensities of (*a*) 0 kV/cm, (*b*) 1.60 kV/cm, and (*c*) 2.05 kV/cm under heightened camera sensitivity (3000 ms exposure time). HL60s lying in Region I are presented with solid curves whereas HL60s lying in Region II are presented with dashed curves. (*d*) Zoomed-in plot of HL60 traces from *c* showing uptake signatures consistent with transient electroporation.

of the electrode gap (Region I of Fig. 5 *b*) and dashed lines represent cells in the region near each electrode (Region II of Fig. 5 *b*). Therefore, solid lines represent cells exposed to slightly lower electric fields than those represented by dashed lines.

In Fig. 6 *c*, four cells internalized greater amounts of PI relative to the other cells shown in the figure (see cells labeled 1–4). A zoomed-in plot of the relatively lightly fluorescing cells is provided in Fig. 6 *d* (i.e., the unlabeled cells from Fig. 6 *c*). Cells labeled 1 and 2 in Fig. 6 *c* reached fluorescence levels that saturated the camera and became untrackable when using a sensitive camera exposure time of 3000 ms. 600 s after PEF exposure, camera sensitivity was reduced to 300 ms to track the cells that saturated the camera. Fig. 7 *a* is a plot of these cells' fluorescence versus time at this decreased camera sensitivity. Cells originally labeled 1–4 in Fig. 6 *c* remain labeled as such in Fig. 7 *a*. The cells exhibiting lower levels of fluorescence remain unlabeled in Fig. 7 *a* and are now buried within the camera noise floor.

For comparative purposes, the fluorescence intensity of saponin-lysed cells was recorded using 30 μM of extracellular PI at both camera sensitivities (300 and 3000 ms exposure times). Using a 3000 ms exposure time, all cellular fluorescence levels of saponin-lysed cells saturated the camera (data not shown). These data show that the cells exhibiting PI uptake characteristics such as the unlabeled cells in Fig. 6, *c* and *d*, internalize much smaller quantities of PI than cells that have been permanently lysed. Using a 300 ms exposure time, permanently lysed cells' fluorescence levels were similar to those labeled 1–4 in Fig. 7 *a* (Fig. 7 *b*).

When PEF exposures were increased beyond $E_n = 2.05$ kV/cm, larger percentages of cells fluoresced at levels saturating the camera when using 3000 ms exposure times. To prevent camera saturation, lower camera sensitivity was used (300 ms exposure time) when more intense PEFs were used. Cellular PI fluorescence intensity versus time is provided in Fig. 8, *a–d*, for experiments using $E_n = 2.05$, 2.88, 3.21, and 3.55 kV/cm, respectively. Again, arbitrary fluorescence units are shown on the left whereas the estimated number of internalized, bound PI molecules is shown on the right vertical axis. The correlation between cellular fluorescence level and the estimated number of internalized, bound PI molecules for Fig. 8 was taken from the 300 ms calibration curve (Fig. 4 *b*). We expect the accuracy of this calibration to decrease as

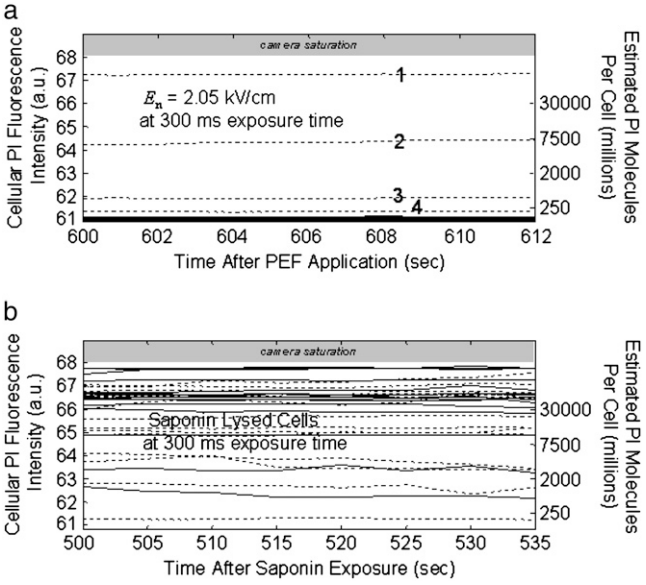

FIGURE 7 (*a*) Continued tracking of cells from Fig. 6 *c* using reduced camera sensitivity (300 ms exposure time). Cells labeled 1–4 are the same cells labeled as such in Fig. 6 *c*. (*b*) HL60s lysed using saponin with a PI concentration of 30 μM fluoresce at intensities similar to those labeled 1–4 in *a*.

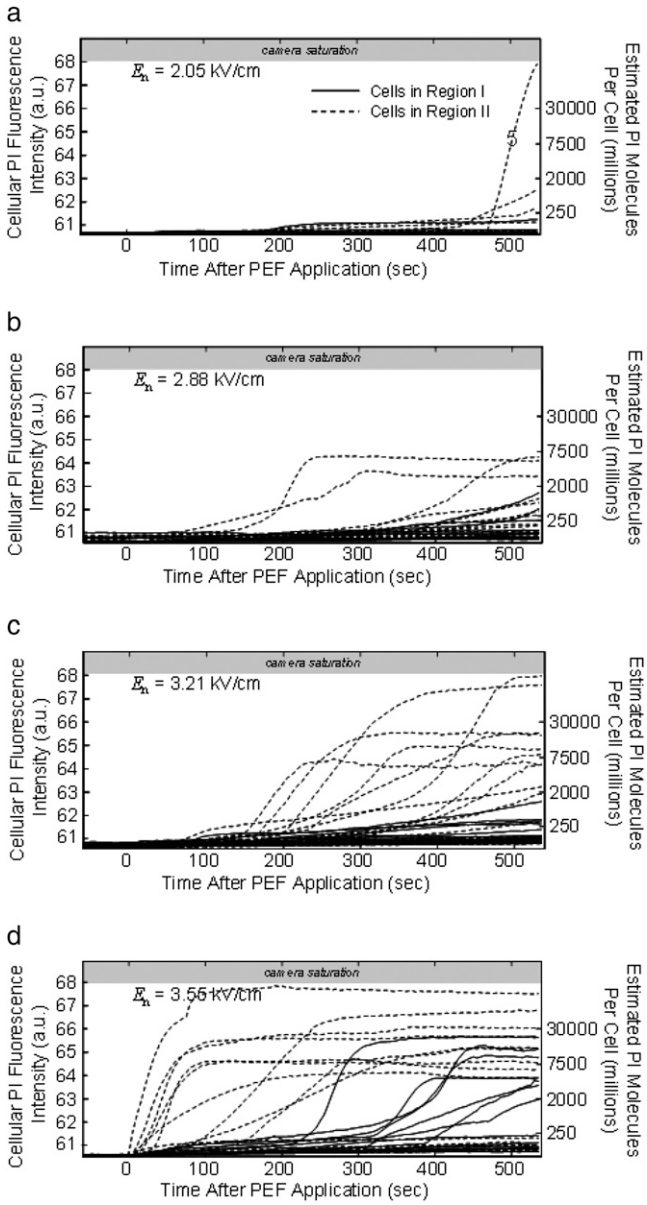

FIGURE 8 PI fluorescence versus time for individual HL60s when exposed to 40 μs PEFs with nominal intensities of (*a*) 2.05 kV/cm, (*b*) 2.88 kV/cm, (*c*) 3.21 kV/cm, and (*d*) 3.55 kV/cm under reduced camera sensitivity (300 ms exposure time). Solid and dashed curves correspond to HL60s lying in Region I and Region II, respectively.

fluorescence levels increase. However, only the qualitative nature of these higher-level PI uptake curves will be important in the ensuing discussion.

DISCUSSION

Influence of field heterogeneity on electroporative cell response

From Figs. 6, *a–c*, and 8, *a–d*, cells lying in Region II generally respond more dramatically to the applied PEF compared to cells lying in Region I. For instance, in Fig. 6 *b*, only cells lying in Region II exhibit detectable amounts of internalized and nucleic acid-bound PI molecules. In Fig. 6 *c*, cells in Region II primarily exhibit higher rates of fluorescence increase at higher fluorescence intensities. In fact, two cells (labeled 1 and 2) fluoresce at intensities saturating the CCD camera. In Fig. 8, where camera sensitivity has been reduced to avoid camera saturation, this trend continues. In Fig. 8 *a*, primarily cells in Region II exhibit fluorescence intensities above the noise floor. In Fig. 8, *c* and *d*, cells in Region II generally fluoresce at greater intensities and reach those intensities sooner. We attribute these trends in electroporative response to the electric field heterogeneity between the microcuvette's electrodes. That is, cells in Region II respond more dramatically to given PEF exposures due to the fact that they are exposed to higher electric field intensities.

The electroporative uptake signatures in a given experiment at first appear inconsistent, exhibiting a broad and inconsistent distribution of responses. However, they become predictable, consistent, and directly correlated to specific field strengths when field heterogeneity is taken into account (analyzed in Fig. 5). Based on our field heterogeneity analysis, we know that HL60s lying in Region II of Fig. 6 *b* are exposed to similar field intensities as HL60s lying in Region I of Fig. 6 *c*. Neglecting overvoltages at the electrode–electrolyte interface, HL60s in Region II of Fig. 6 *b* are exposed to field intensities between 1.6 and 2.03 kV/cm whereas HL60s in Region I of Fig. 6 *c* are exposed to very similar field intensities between 1.78 and 2.05 kV/cm. As a result, their electroporative responses are very similar. Again, HL60s lying in Region II of Fig. 8 *b* (where cells are exposed to between 2.88 and 3.66 kV/cm) respond similarly to those lying in Region I of Fig. 8 *d* (where cells are exposed to similar field intensities, ranging between 3.08 and 3.55 kV/cm).

Categorization and analysis of electroporative uptake signatures

As the electric field intensity used to electroporate HL60s increases, there is an observable progression in electroporative uptake signatures. Starting at 0 kV/cm, in Fig. 6 *a*, HL60s remain at baseline fluorescence levels. In Fig. 6 *b*, as the nominal PEF intensity is increased to 1.60 kV/cm, a number of cells begin to exhibit fluorescence signatures exceeding the noise floor. These cells are exclusively those lying in Region II where field intensities are slightly higher than the nominal field value of 1.60 kV/cm. Therefore we can determine that the threshold for detectible electroporative PI uptake under our experimental conditions is associated with a nominal PEF intensity of ~1.6 kV/cm. It is noted that experiments using lower nominal PEF intensities at even greater camera sensitivities showed no observable PI uptake (data not shown).

When the nominal PEF intensity is raised to 2.05 kV/cm, it can be seen that two characteristically different uptake signatures are produced (Fig. 6 *c*). One uptake signature appears to begin immediately after the PEF and the fluorescence

intensity increases with a decelerating pace, asymptotically stabilizing with relatively low levels of PI uptake (see unnumbered traces in Fig. 6 *c*). The cells exhibiting these uptake signatures are highlighted in a zoomed-in plot of Fig. 6 *c* in Fig. 6 *d*. The kinetics of these uptake signatures are qualitatively similar to those exhibited by cells lying in Region II of Fig. 6 *a* and consistent with the development of transient aqueous pathways in the plasma membrane (i.e., transient electroporation). That is, their decelerating fluorescence signature is consistent with initial electropore development followed by a reduction in total electropore area and/or number over time. Additionally, their relatively low levels of PI uptake suggest a limitation in the duration and size of developed electropores (transient electropores must remain recoverably small (27,28)).

The other electroporative uptake signature observable in Fig. 6 *c* is characterized by immediate but accelerating PI uptake resulting in higher total amounts of PI internalization (see traces labeled 1 through 4). Notice that only cells lying in Region II (where the field intensity is slightly elevated) exhibit this accelerating uptake signature. The kinetics of these uptake signatures are consistent with initial electropore development followed by an accelerating increase in total electropore area and/or number over time (at least during the experimental timescales). By observing these same cells under reduced camera sensitivity later in time (see traces labeled 1–4 in Fig. 7 *a*), it is shown that 600 s after PEF exposure, they have internalized similar amounts of PI as do cells that have been permanently lysed using saponin (Fig. 7 *b*). Taken together, these uptake signatures are suggestive of irreversible electroporative. That is, i), they are associated with higher field intensities that may contribute to electropore expansion beyond recoverability; ii), exhibit increased PI influx over time indicating increased membrane permeability over time; and iii), result in similar amounts of internalized PI as do cells known to be permanently lysed. The design of these particular experiments using the microcuvettes did not allow the study of post-PEF cell viability for a rigorous verification of irreversible electroporation. However, the similarity in PI uptake between the cells exposed to the higher PEF intensities and saponin-lysed cells strongly supports the inferred conclusions.

Delayed onset of accelerated of PI uptake

Inspection of Fig. 8, *a–d*, shows that a number of cells experience a delayed onset of accelerated PI uptake. Deng et al. (29) reported similar responses in ~10 μM, round Jurkat cells under similar environmental conditions (Jurkats suspended in HBSS without Ca^{2+} and Mg^{2+} using a PI concentration of 30 μM) using square PEFs ranging from 60 ns to 100 μs with 50 ns rise times. Delays in observable PI uptake were reported at all experimental pulse widths (60 ns, 300 ns, 10 μs, and 100 μs), although most prevalent when using PEF pulse widths shorter than the predicted plasma membrane charging time constant (tens to hundreds of nanoseconds (23,29)). Delays in observable PI uptake were interpreted as resulting from an electroporative response characterized by i), insufficient initial effect on plasma membrane permeability for efficient PI uptake; and ii), eventual but delayed plasma membrane permeability sufficient for efficient PI uptake due to disruption of intracellular compartments. This organelle disruption may lead to delayed apoptotic plasma membrane permeability, for instance, by elevating cytosolic Ca^{2+} levels through endoplasmic reticulum rupture (9) that is known to be a key factor in triggering apoptotic pathways (30). This interpretation is also consistent with a number of theories on electroporative dynamics for submicrosecond pulse widths (18,19,28), but does not address the observation of delayed PI uptake when using 10 and 100 μs PEFs.

We observed delayed responses using PEF pulse widths longer than the plasma membrane charging time constant, although only when exposed to a limited range of PEF intensities (see for instance several traces in Fig. 8, *a–d*). These delayed responses are not necessarily the result of an extended period of time after PEF exposure marked by PI impenetrability. Rather, we assert that the apparent delays observed here are associated with the time required for a sufficient amount of PI to diffusively transport across the plasma membrane to reach detectible fluorescence levels. It is striking that elevation of cellular fluorescence beyond the noise floor is often associated with an abrupt acceleration in PI uptake that is sometimes delayed, in some cases, by hundreds of seconds after PEF exposure. Take for instance the trace that is labeled ''5'' in Fig. 8 *a*. At this reduced camera sensitivity (300 ms exposure time), PI fluorescence of that cell does not exceed the noise floor until ~480 s after PEF exposure. This indicates an abrupt increase in membrane permeability ~480 s post-PEF exposure. However, this cell is likely internalizing low levels of PI (that are undetectable when using a 300 ms camera exposure time) before this abrupt change in PI influx. To substantiate this point, it can be seen from Fig. 6 *c* that HL60s under identical experimental conditions begin internalizing detectible amounts of PI when a higher camera sensitivity is used (see traces labeled 1–4). HL60s lying in Region II of Fig. 6 *c* likely internalize PI in similar manners to those in Region II of Fig. 8 *a* and appear differently due only to the change in camera sensitivity. Therefore, we infer that there exists a set of conditions where relatively small electropores may remain stable for hundreds of seconds while facilitating relatively low levels of PI uptake. These quasi-stable electropores may expand abruptly, possibly beyond the point of recovery, manifesting as a rapid increase in PI fluorescence. It is unclear what interplay of membrane molecular dynamics, cytoskeletal dynamics, and/or active physiological mechanisms might produce such forms of PI uptake, although a sound explanation of these delayed accelerative uptake signatures will likely necessitate expanding beyond traditional electroporation theory.

Identification of a transient electroporation window

Although it is uncertain what underlying dynamics are responsible for delayed, accelerating PI uptake, the uptake signature characterized by low-level, decelerating uptake (e.g., those shown in Fig. 6 *c*) is likely associated with transient electroporation. We observed this form of PI uptake under our experimental conditions between PEF intensities of 1.6 and 2 kV/cm. Although it remains possible that PEF exposures beyond 2 kV/cm result in transient plasma membrane PI permeability, the range in PEF intensities between 1.6 and 2 kV/cm serves as a ''window'' providing a high probability of inducing transient electroporation under our experimental conditions. Based on our quantitative analysis, cells exhibiting PI uptake signatures consistent with transient electroporation fluoresce at levels indicating 88.3 $\pm$ 20.9 million internalized and nucleic acid-bound PI molecules per cell ($N = 12$). Future studies will explore the influence of a number of experimental factors on this quantity of PI uptake.

Analysis of transient electropore persistence

PI uptake signatures consistent with transient electroporation appear to level off 500–600 s after PEF exposure (Fig. 6, *b* and *c*). This leveling is associated with a number of factors including electropore closure, intracellular PI diffusion, and the equilibrium of PI-nucleic acid associative dynamics. However, based on this data, we are able to infer an estimated upper bound on transient electropore persistence at 500–600 s under our experimental conditions.

Spatially regulated PI uptake exploiting field heterogeneity

A final PI uptake experiment was conducted to determine if the spatial variability in field intensity between the microcuvette's electrodes was capable of preferentially affecting the response of individual cells in suspension or even different portions of individual cells. Here, a 40 μs, 1.92 kV/cm PEF was applied to HL60s with camera settings set for increased sensitivity. This PEF intensity was chosen in an attempt to induce high levels of plasma membrane permeability next to the nearest electrode. Results can be seen in Fig. 9. The image in the top left is an optical image of the cells before PEF exposure where the anode can be seen on the right and the cathode can be seen on the left. In the remaining pictures, fluorescent images of the cells between 5 and 35 s after PEF exposure are presented. Arrows are provided to draw attention toward two cells whose PI fluorescence distribution indicates that the PI uptake was asymmetrical. That is, on these individual cells, the data shows that PI uptake was accelerated in the cells' hemisphere adjacent to the nearest electrode where the electric field gradient is the strongest.

The possibility of using electric field heterogeneity to spatially regulate electroporative responses is exciting in that there are a number of potential applications (e.g., tumor ablation and controlled gene and drug delivery). Our microcuvette was not designed to provide heterogeneous electric fields to cells, although electrode geometries can be designed to provide better control over localized molecular delivery. Additionally, investigators should be aware of how sensitive electroporative response is to electric field gradients that are often unavoidable in traditional electroporation apparatus. This issue becomes particularly important if conclusions are to be made from observation of preferential cathodic and/or anodic plasma membrane effects. These have been discussed frequently in previous studies (31–38).

CONCLUSIONS

We have obtained experimental data quantitatively characterizing electroporative uptake kinetics in HL60 human leukemia cells resulting from 40 μs PEF exposures successfully. Uptake kinetics were used to identify a range in PEF intensities resulting in transient electroporation. Cells exposed to PEFs between 1.6 and 2 kV/cm exhibited PI uptake signatures consistent with transient electroporation and internalized ~88 million PI (bound) molecules per cell. We have also identified a high level, accelerating PI uptake signature that is associated with field intensities between 2 and 3 kV/cm. This accelerating uptake signature is unexplainable through traditional electroporation theory alone. Finally, we have analyzed the electric field heterogeneity between the electrodes of our electroporation device and used this information to correlate trends in PI uptake to the distribution in electric field. Field heterogeneity was also used to spatially regulate PI uptake.

This work will provide useful experimental data in validating and improving electroporation models. It also underscores the need to conduct more experiments with a number of focuses. First, it will be important to catalog electroporative uptake kinetics for a wide variety of experimental parameters: for instance, PEF duration, PEF intensity, PEF shape (waveform characteristics), PEF number and separation time, molecular size, molecular structure, and environmental conditions (e.g., suspension conductivity and composition). The system developed to carry out the experiments described here affords the capability of experimentally examining a broad range of these electroporation topics. Future work also will address electropore persistence explicitly.

APPENDIX: MICROCUVETTE FABRICATION

We used 1 inch $\times$ 3 inches $\times$ 0.040 inch microscope slides (Evaporated Metal Films, Ithaca, NY) precoated with a 5 nm titanium (Ti) adhesion layer and a 100 nm gold (Au) top layer as substrates for subsequent processing. AZ P4620 photoresist (AZ Electronic Materials, Somerville, NJ) was spun onto

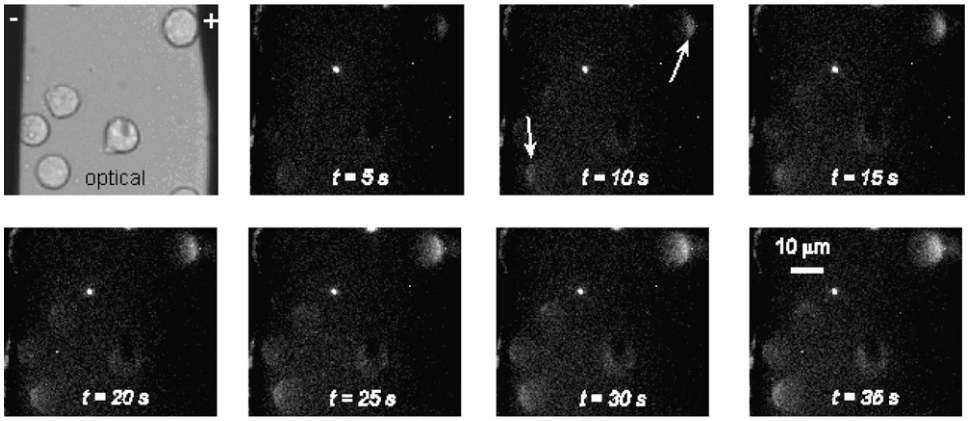

FIGURE 9 Images of HL60s during an experiment designed to elicit asymmetrical PI uptake by using the electric field gradients near each electrode. (*Top left*) Optical image of HL60s before PEF application. Other images are fluorescent images of HL60s at the indicated times after PEF exposure. Arrows indicate hemispherical asymmetry in PI uptake.

the Au top layer of an individual substrate at 500 rpm for 45 s to yield a photoresist layer thicker than 20 μm (31) (Fig. 10 *a*). The photoresist-coated substrate was then softbaked on a hotplate at 110°C for 2 min and 15 s to slightly harden the photoresist. The photoresist coated substrate was then exposed to ultraviolet (UV) light (at an intensity of $I_{UV} = 7.5$ mW/cm^2 for a duration of $t = 50$ s) using a Karl Suss MJB-3 contact aligner under a mask

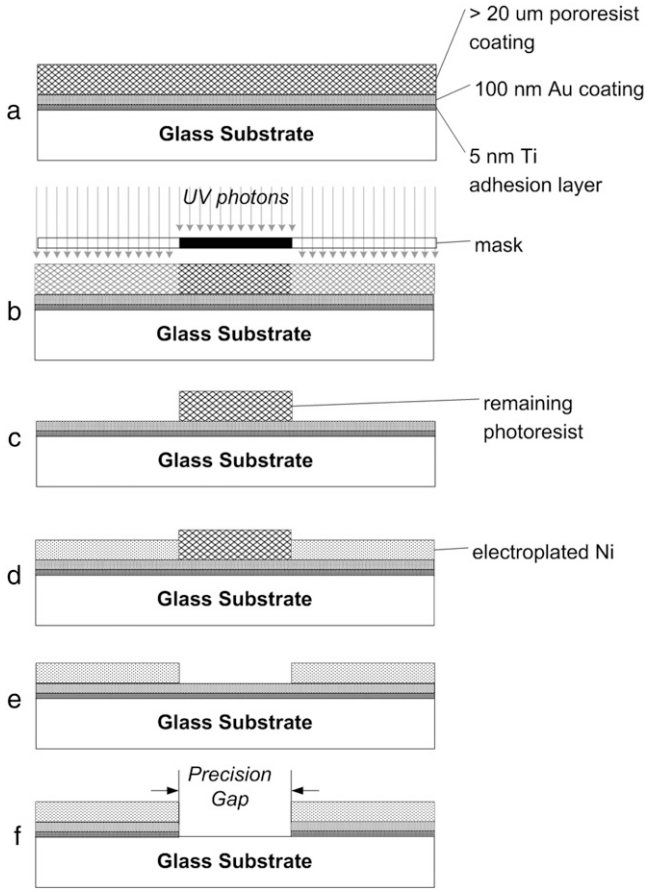

FIGURE 10 Schematic illustrating microcuvette fabrication technique. (*a*) Application of photoresist to glass-Ti-Au substrate. (*b*) Masked UV exposure. (*c*) Device after photoresist development. (*d*) Ni electroplating of electrodes. (*e*) Elimination of photoresist using acetone. (*f*) Chemical etching of Ti-Au coatings leaving a precision electrode gap.

that allowed the positive photoresist to be exposed to UV only in the location of the future electrodes (Fig. 10 *b*). This masked UV exposure ensured that only the photoresist coating in the future electrode region would become soluble in a developer solution. The device was then submerged in the developer solution composed of AZ 400K developer (AZ Electronic Materials) mixed 2:5 with deionized water, until the last of the photoresist in the electrode region vanished (Fig. 10 *c*). The device was then hardbaked in an oven at 120°C for 15 min to fully harden the remaining photoresist.

Metal electrodes were then electroplated to the Au exposed areas on the substrate (Fig. 10 *d*). Nickel (Ni) was chosen as the electrode metal due to convenience, although any metal capable of electroplating may be used to construct the microcuvette electrodes. A Ni plating thickness of $\sim$20 μm was chosen to fully contain a variety of cell types. In principle, any electrode thickness may be applied, as long as the developed photoresist pattern is thicker than the desired electrode thickness. Ni electroplating was carried out in a manner identical to that described in (39) where devices were submerged in a 50°C MicroFab NI 100 sulfamate bath (Enthone, West Haven, CT). A submerged nickel gauze was used as the nickel source and was connected to the anode end of a power supply with a sufficient current rating. Electroplating current density was set to 0.517 mA/mm^2 to achieve plating rates of 1 μm/min (40). It should be noted that Ni toxicological studies were not carried out here. The question of Ni toxicity will be addressed in future studies either by creating gold microcuvette electrodes or electroplating gold over the current microcuvette's Ni electrodes.

After electroplating, the remaining photoresist was removed by soaking the device in an acetone bath until no trace of photoresist was observed (Fig. 10 *e*). The Au top layer between the Ni electrodes was removed by soaking the device in Gold Etchant GE-8148 (Transene Company, Danvers, MA) that does not etch glass or Ni (41). Typical soaking times required to remove the entire Au layer were $<$5 min. The device was then rinsed for at least 10 min in deionized water. The remaining 5 nm Ti adhesion layer between the electrodes was dissolved in buffered hydrofluoric acid mixed 1:100 HF to H_2O. Although HF also etches glass, the Ti layer is so thin that the device may be removed from the buffered HF with the Ti layer fully removed but before any detectable damage has occurred to the glass. The typical buffered HF soaking time was 4 min. Next, the device was rinsed for at least 10 min in deionized water. With the Au and Ti layers fully removed from the region between the Ni electrodes, microscope light may penetrate freely the region between the electrodes (Fig. 10 *f*).

The authors thank Abhishek Agarwal, Swomitra Mohanty, and Professor Hongrui Jiang, whose kind assistance made development of the microcuvette possible. The authors also thank Michael Hitchcock for his work in the clean rooms, Rafael Viloria for helping maintain our HL60 cell line, and Alireza Mashal for his data acquisition expertise.

This work was supported by the Air Force Office of Scientific Research FY01 ''Radiofrequency Bioeffects'' MURI program through a consortium grant with Old Dominion University.

REFERENCES

1. Weaver, J. C. 2000. Electroporation of cells and tissues. *IEEE Trans. Plasma Sci.* 28:24–33.
2. Neumann, E., A. E. Sowers, and C. A. Jordan, editors. 1989. Electroporation and Electrofusion in Cell Biology. Plenum Press, New York.
3. Zimmerman, U., and G. A. Neil. 1996. Electromanipulation of Cells. CRC Press, Boca Raton, FL.
4. Chang, C. C., B. M. Chassy, J. A. Saunders, and A. E. Sowers. Eds. 1992. Guide to Electroporation and Electrofusion. Academic Press, San Diego.
5. Rubinsky, B. 2007. Irreversible electroporation in medicine. *Technol. Cancer Res. Treat.* 6:255–259.
6. Esser, A. T., K. C. Smith, T. R. Gowrishankar, and J. C. Weaver. 2007. Towards sold tumor treatment by irreversible electroporation: intrinsic redistribution of fields and currents in tissue. *Technol. Cancer Res. Treat.* 6:261–273.
7. Rubinsky, B., G. Onik, and P. Mikus. 2007. Irreversible electroporation: a new ablation modality—clinical implications. *Technol. Cancer Res. Treat.* 6:37–48.
8. Nuccitelli, R., U. Pliquett, X. Chen, W. Ford, R. J. Swanson, S. J. Beebe, J. F. Kold, and K. H. Schoenbach. 2006. Nanosecond pulsed electric fields cause melanomas to self-destruct. *Biochem. Biophys. Res. Commun.* 343:351–360.
9. Beebe, S. J., P. M. Fox, L. J. Rec, K. Somers, R. H. Stark, and K. H. Schoenbach. 2002. Nanosecond pulsed electric field (nsPEF) effects on cells and tissues: apoptosis induction and tumor growth inhibition. *IEEE Trans. Plasma Sci.* 30:286–292.
10. Beebe, S. J., P. M. Fox, L. J. Rec, E. L. Willis, and K. H. Schoenbach. 2003. Nanosecond, high-intensity pulsed electric fields induce apoptosis in human cells. *FASEB J.* 17:1493–1495.
11. Beebe, S. J., J. White, P. F. Blackmore, Y. Deng, K. Somers, and K. H. Schoenbach. 2003. Nanosecond pulsed electric fields modulate cell function through intracellular signal transduction mechanisms. *Physiol. Meas.* 25:1077–1093.
12. Andre, F. L., and M. Mir. 2004. DNA electrotransfer: its principles and an updated review of its therapeutic applications. *Gene Ther.* 11:S33–S42.
13. Nishi, T., K. Yoshizato, S. Yamashiro, H. Takeshima, K. Sato, K. Hamada, I. Kitamura, T. Yoshimura, H. Saya, J. Kuratsu, and Y. Ushio. 1996. High-efficiency in vivo gene transfer using intraarterial plasmid DNA injection following in vivo electroporation. *Cancer Res.* 56:1050–1055.
14. Hu, Q., V. Sridhara, R. P. Joshi, J. F. Kolb, and K. H. Schoenbach. 2006. Molecular dynamics analysis of high electric pulse effects on bilayer membranes containing DPPC and DPPs. *IEEE Trans. Plasma Sci.* 34:1405–1411.
15. Wells, D. J. 2004. Gene therapy progress and prospects: electroporation and other physical methods. *Gene Ther.* 11:1363–1369.
16. Wu, C.-M., M. W. Lin, J. T. Cheng, Y. M. Wang, Y. W. Huang, W. Z. Sun, and C. R. Lin. 2004. Regulated, electroporation-mediated delivery of pro-opiomelanocortin gene suppresses chronic constriction injury-induced neuropathic pain in rats. *Gene Ther.* 11:933–940.
17. Heller, R. 2002. The development of electroporation. *Science.* 295:277.
18. Gowrishankar, T. R., and J. C. Weaver. 2006. Electrical behavior and pore accumulation in a multicellular model for conventional and supra-electroporation. *Biochem. Biophys. Res. Commun.* 349:643–653.
19. Vasilkoski, J., A. T. Esser, T. R. Gowrishankar, and J. C. Weaver. 2006. Membrane electroporation: the absolute rate equation and nanosecond time scale pore creation. *Phys. Rev. E.* 74:021904.
20. Tieleman, D. P. 2006. Computer simulations of transport through membranes: passable diffusion, pores, channels and transporters. *Clin. Exp. Pharmacol. Physiol.* 33:893–903.
21. Pavlin, M., V. Leben, and D. Miklavcic. 2007. Electroporation in dense cell suspension—Theoretical and experimental analysis of ion diffusion and cell permeabilization. *Biochim. Biophys. Acta.* 1770:12–23.
22. Joshi, R. P., V. Sridhara, and K. H. Schoenbach. 2006. Microscopic calculations of local lipid membrane permitivities and diffusion coefficients for application to electroporation analyses. *Biochem. Biophys. Res. Commun.* 348:643–648.
23. Ji, Z., S. M. Kennedy, J. H. Booske, and S. C. Hagness. 2006. Experimental studies of persistent poration dynamics of cell membranes induced by electric pulses. *IEEE Trans. Plasma Sci.* 34:1416–1424.
24. Fletcher, G. G., F. E. Rossetto, J. D. Turnbeull, and E. Nielboer. 1994. Toxicity, uptake and mutagenicity of particulate and soluble nickel compounds. *Environ. Health Perspect.* 102:69–79.
25. Orlowski, S., J. Belehradek, Jr., C. Paoletti, and L. M. Mir. 1988. Transient electropermeabilization of cells in culture. Increase of the cytotoxicity of anticancer drugs. *Biochem. Pharmacol.* 37:4727–4733.
26. Müller, K. J., V. L. Sukhorukov, and U. Zimmermann. 2001. Reversible electropermeabilization of mammalian cells by high-intensity, ultra-short pulses of submicrosecond duration. *J. Membr. Biol.* 184:161–170.
27. Joshi, R. P., and K. H. Schoenbach. 2000. Electroporation dynamics in biological cells subjected to ultrafast electrical pulses: A numerical simulation study. *Phys. Rev. E.* 62:1025–1033.
28. Joshi, R. P., Q. Hu, and K. H. Schoenbach. 2003. Dynamic modeling of cellular response to short-duration, high-intensity electric fields. *IEEE Trans. Dielectrics Electr. Insul.* 10:778–787.
29. Deng, J., K. H. Schoenbach, E. S. Buescher, P. S. Hair, P. M. Fox, and S. J. Beebe. 2003. The effects of intense submicrosecond electrical pulses on cells. *Biophys. J.* 84:2709–2714.
30. Demaurex, N., and C. Distelhorst. 2003. Apoptosis—the calcium connection. *Science.* 300:135–139.
31. Rols, M.-P., and J. Teissié. 1990. Electropermeabilization of mammalian cells. *Biophys. J.* 58:1089–1098.
32. Tekle, E., R. D. Astumian, and P. B. Chock. 1994. Selective and asymmetric molecular transport across electroporated cell membranes. *Proc. Natl. Acad. Sci. USA.* 91:11512–11516.
33. Gabriel, B., and J. Teissié. 1997. Direct observation in the millisecond time range of fluorescent molecule asymmetrical interaction with the electropermeabilized cell membrane. *Biophys. J.* 73:2630–2637.
34. Gabriel, B., and J. Teissié. 1999. Time course of mammalian cell electropermeabilization observed by millisecond imaging of membrane property changes during the pulse. *Biophys. J.* 76:2158–2165.
35. Tekle, E., R. D. Astumian, W. A. Friauf, and P. B. Chock. 2001. Asymmetric pore distribution and loss of membrane lipid in electroporated DOPC vesicles. *Biophys. J.* 81:960–968.
36. Golzio, M., M. P. Rols, and J. Teissié. 2004. In vitro electric field-mediated permeabilization, gene transfer, and expression. *Methods.* 33:126–135.
37. Phez, E., C. Faurie, M. Golzio, J. Teissié, and M.-P. Rols. 2005. New insights in the visualization of membrane permeabilization and DNA/membrane interaction of cells submitted to electric pulses. *Biochim. Biophys. Acta.* 1724:248–254.
38. Vernier, P. T., Y. Sun, and M. A. Gundersen. 2006. Nanoelectropulse-driven membrane perturbation and small molecule permeabilization. *BMC Cell Biol.* 7:37.
39. Agarwal, A. K., S. S. Sridharamurthy, D. J. Beebe, and H. Jiang. 2005. Programmable autonomous micromixers and micropumps. *J. Microelectromech. Syst.* 14:1409–1421.
40. Microfab NI 100 sulfamate nickel for semiconductor processing technical data sheet. 2002. Enthone Incorporated, West Haven, CT.
41. Etchant/Metal compatibility chart. 2005. Transene Company, Danvers, MA.